TRANSPORT PHENOMENA AND FLUID MECHANICS

AIChE JOURNAL

Bending and low-frequency vortex shedding of flexible cylinders in laminar shear flow

Jos J. Derksen [ORCID]

School of Engineering, University of Aberdeen, Aberdeen, UK

Correspondence
Jos J. Derksen, School of Engineering, University of Aberdeen, Aberdeen, UK.
Email: jderksen@abdn.ac.uk

Abstract

Simulations of the interaction between flexible cylinders attached to a solid surface and a laminar shear flow have been performed. The flow simulations fully resolve the geometrical details and are based on the lattice-Boltzmann method. An immersed boundary method is used to impose the no-slip conditions at the cylinder surfaces and to determine the distribution of hydrodynamic forces over the cylinder. The latter are responsible for the bending deformation of the cylinders. We first study simple shear systems under steady conditions for which experimental data are available that we use for validation. We then study flexible cylinders in Poiseuille flow that exhibit vortex shedding and demonstrate that the flexibility of the cylinders has a pronounced effect on the temporal behavior of the flow system.

KEYWORDS
bifurcation, fluid–structure interaction, lattice-Boltzmann method, particle-resolved simulation, shear flow, vortex shedding

1 | INTRODUCTION

Fluid–structure interaction (FSI) is a topic with extensive implications in natural and man-made systems and playing out on a vast range of length scales. On one side of the length scale spectrum, there are the interactions between large engineered structures such as bridges and high-rise buildings with an airflow surrounding them that have length scales of tens to hundreds of meters. As an example on the opposite, microscopic, side: at the intracellular level, the cytoskeleton interacts with the flow of cytosol, the liquid inside cells, at scales of tens to hundreds of nanometers. In between these eight to ten orders of magnitude there is a rich collection of phenomena that involve FSI: deformation of red blood cells in hemodynamics,[1,2] flow–plant interactions in biomechanics,[3,4] vortex-induced vibrations of cylinders in cross flow,[5] and flight of insects and birds and airplanes[6,7] to name just a few.

A number of physics-related distinctions in FSI are relevant. At small length scales—roughly up to the submillimeter level—flow dynamics are well captured by the Stokes equations. Many microscopic biological systems fall in this category.[8] Extensive experimental and modeling research has been done on—for example—motion of fibrous bacteria through liquids.[9] At larger scales, the effects of fluid inertia become appreciable with the Navier–Stokes equations governing fluid flow and eventually—at still larger scales—leading to turbulence as an important component of FSI, for example, in flow–plant interaction.[3] The elastic properties of the structural components of FSI also give rise to various classes of phenomena. This can be appreciated in terms of the natural frequencies of the structures in relation to the time scales of the fluid flow. For instance, if the eigenfrequencies of structural elements are much higher than the frequencies associated to the temporal behavior of the fluid flow, the latter governs the time-dependent behavior of the entire system with

---

the structural elements following the flow in a quasi-static manner. Inertial effects of the structural elements are then unimportant. In other cases, FSI results in a strong interference between structural and fluid flow time scales. Many systems that involve vortex-induced vibrations are examples of the latter.[5]

The present article deals with detailed numerical simulations of FSI at an intermediate length scale of the order of millimeters. It is inspired by experimental work on soft hair beds by Alvarado et al[10] in which they show nonlinear behavior as a direct consequence of linear elastic cylinders ("hairs") bending under the influence of a laminar shear flow. Soft hair beds are encountered in biology; in humans, in blood vessels and intestines. Since they play a role in regulating fluid flow and mass transfer at the microscale, they also might be relevant in (nature-inspired) applications in chemical engineering.

In the experimental work,[10] a Couette flow of a Newtonian liquid between two parallel solid surfaces was created with the flexible cylinders attached to one of the surfaces in a regular pattern. The shear stress was measured as a function of the shear rate. The authors observed apparent shear-thinning behavior as a result of the hairs bending under the influence of the shear flow, which then leaves more room for fluid flow above the hairs and thus a sublinear relation between shear rate and shear stress. These were experiments at low Reynolds numbers with a steady stimulus (shear rate) and steady response (shear stress).

It is well known that beyond a certain Reynolds number the flow past cylinders develops time-dependent instabilities known as vortex shedding.[11] We have an interest in studying—through detailed simulations—how flexible cylinders in soft hair beds respond to flow conditions for which vortex shedding occurs. This interest stems from questions about the impact of vortex shedding on the overall drag of the soft hair beds as well as the role vortex shedding could play in mixing and mass transfer of the unsteady fluid flow through and above the hair beds.

Our particle-resolved numerical approach for flexible cylinders in fluid flow has been developed recently.[12] It has been verified and validated for a few special cases. In the present paper, first, the steady-state experimental results by Alvarado et al[10] have been used for further validation of the computational methodology. The main aim of the paper is, however, to show how flexibility of the cylinders influences the dynamics of soft hair beds under laminar conditions for which vortex shedding occurs.

There is—of course—a vast body of literature on vortex shedding behind a single, rigid cylinder and also on vortex shedding behind arrangements of multiple cylinders. For the latter situations, the vortex patterns and shedding frequencies have been mapped out as a function of "gap ratios" and Reynolds numbers, mostly based on numerical simulations.[13-15] Where for a single cylinder onset of vortex shedding occurs at a Reynolds number of ~50, systems with multiple cylinders can show—dependent on how the cylinders are arranged—significantly lower critical Reynolds numbers.[15]

Given the experiments by Alvarado et al[10] that involve flexible cylinders arranged in regular arrays in a Taylor–Couette device, our simulations apply periodic boundaries in the streamwise and spanwise directions and no-slip walls in the third direction with flexible cylinders clamped on the bottom wall to mimic soft hair beds experiencing shear. In the simple-shear (Couette) simulations, the top wall is moving parallel to the bottom wall. In the simulations that involve vortex shedding, the flow is driven by a pressure gradient, and the top and bottom wall are static (planar Poiseuille flow).

The organization of the article is as follows. In the next section, the flow systems will be introduced. We then give a brief account of the numerical methods that have been applied and discuss the choice of numerical parameters. The results of the simulations of Alvarado et al[10] validation case will be presented next, after which we will go into the simulations that involve vortex shedding. First—as a reference—two-dimensional vortex shedding and then three-dimensional. At the end of the article, conclusions will be reiterated and options for future research discussed.

2 | FLOW SYSTEM

Two flow configurations have been considered: A shear flow system that mimics the experimental study of Alvarado et al,[10] and a planar Poiseuille flow in which the cylinders induce vortex shedding. The flow configurations along with a Cartesian coordinate system are shown in Figure 1. They consist of a rectangular volume $L \times W \times H$ with no-slip walls at top $z = H$ and bottom $z = 0$. One or more flexible cylinders with diameter d, length ℓ, and bending stiffness EI are attached to the bottom wall. The domains contain a Newtonian liquid that has density ρ and kinematic viscosity ν. In the simple shear system, flow in the x-direction is generated by moving the top wall with a constant velocity U_w in the positive x-direction. The Poiseuille flow
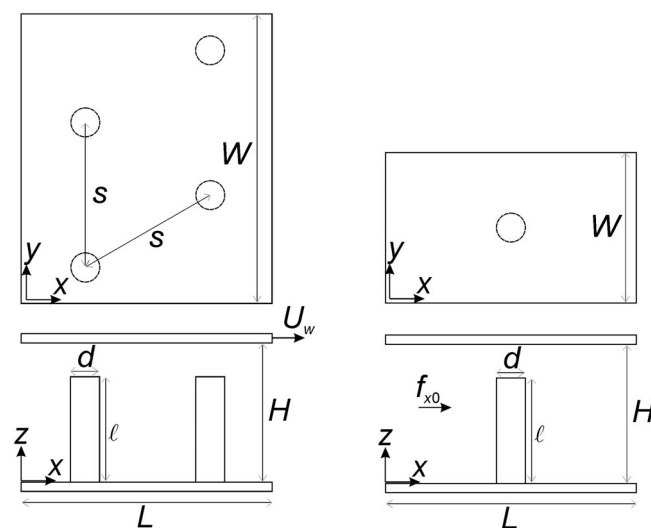

FIGURE 1 Flow geometries including coordinate systems. Both geometries are periodic in x and y directions. Left: top and side view of the simple-shear system with—in this case—cylinders placed in a periodic hexagonal arrangement with $W = 2s$ and $L = \sqrt{3}s$. Right: top and side view of the planar Poiseuille system with one cylinder and the flow driven by a uniform body force f_{x0}

system is driven by a uniform body force (force per unit volume) f_{x0} acting in the positive x-direction. Periodic boundary conditions apply in the x (streamwise) and y (spanwise) directions. This mimics an infinite, two-dimensional array of cylinders.

For reference, as well as to relate to findings in the literature, we also will report briefly on two-dimensional simulations in the xy plane (refer to Figure 1) and homogeneous conditions in the z-direction. They will teach us about the onset of vortex shedding by infinitely long rigid cylinders in a periodic configuration.

The flow systems as described above have been characterized and analyzed mostly in dimensionless terms. Conditions are such that even in the absence of cylinders, the flow in between the no-slip walls is laminar. The shear flow has Reynolds numbers $\mathrm{Re}_w = \frac{U_w H}{\nu}$ of order 10. Without cylinders, the Poiseuille flow has superficial velocity $U_0 = \frac{f_{x0} H^2}{12 \rho \nu}$. The average superficial velocity (with cylinder[s] present) is denoted by the symbol U. These definitions give rise to the following Reynolds numbers: $\mathrm{Re}_0 = \frac{U_0 d}{\nu} = \frac{f_{x0} H^2 d}{12 \rho \nu^2}$, $\mathrm{Re}_{ch} = \frac{UH}{\nu}$ (Reynolds number based on the channel height) and $\mathrm{Re} = \frac{Ud}{\nu}$ that are all well below 200 in this study. Note that only Re_w and Re_0 are based on input parameters; the velocity U is an output parameter and so are Re and Re_{ch}.

The flexibility of the cylinder has been characterized by its bending stiffness EI with E Young's modulus and I the moment of inertia of the cross-sectional area of the cylinder ($I = \pi d^4/64$). Dimensionless flexibility for Poiseuille flow systems has been defined as $\chi = \rho U^2 \ell^4 / EI$. This can be interpreted in terms of beam deflections. A clamped cylinder experiencing a uniform load (force per unit length) q deflects at its free tip by $\delta = \frac{1}{8} q \ell^4 / EI$. If we scale q with $\rho U^2 d$ then χ is a scale for cylinder deflection relative to the cylinder's diameter.

For the shear flow systems, we follow the scaling procedures and notation of Alvarado et al.[10] The authors of Alvarado et al[10] define a rescaled velocity as $\tilde{v} = \frac{\rho \nu \ell^2 U_w}{E \phi d^2 H} \left(1 - \frac{\ell}{H}\right)^{-3/2}$ with ϕ the hair area packing fraction, i.e. the fraction of the bottom surface area occupied by cylinders. Rescaled velocity is an input parameter to the simulations and includes the bending stiffness of the cylinders. With increasing $\tilde{v}$, bending increases.

Vortex shedding gives rise to periodic fluctuations with frequencies for which the symbol f has been used. This defines a Strouhal number $\mathrm{St} = fd/U$. When it comes to vortex shedding, this article is concerned with "slow" fluctuations. In this respect, slow means that the frequencies induced by the flow are much smaller than the first natural frequency of a clamped beam, which is $f_{n1} \approx 2\pi \cdot 1.875^2 \cdot \sqrt{\frac{EI}{\rho_s \frac{\pi}{4} d^2 \ell^4}}$[16] with ρ_s the density of the cylinder material. "Slow" then implies $f/f_{n1} \ll 1$. In physical terms, it means that the inertial effects of the cylinder associated with its deformation can be discarded.

A list of dimensionless numbers—including definitions—is provided in Table 1.

3 | SIMULATION METHOD AND NUMERICAL SETTINGS

The simulations described in this article build on earlier work of ours on particle-resolved simulations involving nonspherical particles.

TABLE 1 Definitions of dimensionless numbers

Expression	Description
$\mathrm{Re}_w = U_w H / \nu$	Couette flow Reynolds number
$\mathrm{Re}_{ch} = UH / \nu$	Channel flow Reynolds number
$\mathrm{Re} = Ud / \nu$	Cylinder Reynolds number based on superficial velocity U
$\mathrm{Re}_0 = U_0 d / \nu$	Cylinder Reynolds number based on Poiseuille flow velocity U_0
$\chi = \rho U^2 \ell^4 / EI$	Flexibility parameter
$\mathrm{St} = fd/U$	Strouhal number
$\tilde{v} = \frac{\rho \nu \ell^2 U_w}{E \phi d^2 H} \left(1 - \frac{\ell}{H}\right)^{-3/2}$	Rescaled velocity (according to Alvarado et al[10])
$\tilde{Z} \equiv \frac{Z - Z_\infty}{Z_0 - Z_\infty}$	Rescaled impedance (according to Alvarado et al[10])

Bending flexibility of cylindrical particles was introduced in Derksen.[12] Here, we give a brief overview of the numerical methodology and refer to Derksen[12] for the details.

Fluid flow is solved by the lattice-Boltzmann (LB) method, more specifically the scheme that has been introduced in Somers[17] and Eggels and Somers.[18] This scheme discretizes three-dimensional space with a uniform cubic lattice of cells with side length Δ and provides velocity and pressure data at points in the centers of each cell. The scheme evolves explicitly in time with a time step Δt. The top and bottom wall are aligned with the lattice and no-slip is imposed there by a half-way bounce-back process.[19] No-slip conditions on other surfaces—notably the surfaces of the deforming cylinders—have been imposed by an immersed boundary (IB) method.[20] In this method, a cylinder surface is defined by a set of closely spaced marker points. The spacing between these points typically is 0.5Δ. Our version of the IB method is based on forcing.[21] At each marker point we determine, by linear interpolation from the lattice points, the velocity. We then locally apply a force on the fluid so as to make its velocity at the marker point approach the required velocity of the solid surface at that marker point. For a static solid surface, the required velocity would be zero.

As a result, this forcing-based IB method not only imposes the no-slip condition at the cylinder surfaces, it also provides the distribution of forces exerted by the fluid flow over the cylinder surface. This hydrodynamic force distribution then allows for determining the bending deformation of the cylinder.[12] It must be noted that this is a process that tightly couples cylinder deformation and fluid flow. The fluid flow induces deformation of the cylinder with the deformation impacting the fluid flow as a result of the cylinder changing shape.

In determining the deformation of the cylinder, we make two major assumptions: quasi-static deformations and small deformations. The quasi-static assumption implies that the deformation responds instantaneously to a changing hydrodynamic load. This is a justified approach if the natural frequencies of the cylinder are much larger than those associated with the hydrodynamics, in this case vortex shedding. The small deformations assumption allows for relatively

simple relationships between force distributions and bending moments and between bending moments and deflections.[22]

Previous work has assessed the impact of numerical settings on the outcomes of simulations.[12] Also, in this article, we will perform such assessments. Most importantly, this is about spatial and temporal resolution of the simulations. Spatial resolution is then expressed in the number of grid spacings spanning a cylinder diameter. As a default resolution, we will be using $d = 16\Delta$. For collections of rigid cylinders, this has proven to be an adequate resolution for cylinder-based Reynolds numbers of order 10 in view of comparisons with simulations that had $d = 12\Delta$ and $d = 24\Delta$.[23] This also was the case for a single flexible cylinder settling under gravity.[12] Since—in principle—vortex shedding might pose specific resolution challenges, also in this article some simulations at the default $d = 16\Delta$ are compared to those with $d = 12\Delta$ and $d = 24\Delta$.

Temporal resolution is such that the viscous time scale d^2/ν comprises $1.02 \cdot 10^4$ time steps. Also, the effect of this choice has been tested by performing simulations that have significantly less time steps per viscous time scale. The length of a typical simulation is 20–40 viscous time scales, that is, in the range of $2 \cdot 10^5$ to $4 \cdot 10^5$ time steps.

The bending of cylinders is accomplished by dividing the cylinder into equal-size segments along its centerline. Previous work has assessed the sensitivity with respect to the number of segments per cylinder.[12] Based on the results of this assessment, we will be using segments with a length of $0.25d$ throughout this paper, that is, 20 segments over a cylinder with $\ell/d = 5$.

For the Poiseuille flow systems, we define a base-case. It has aspect ratios $L/d = 20$, $W/d = 5$, $H/d = 6.25$, and $\ell/d = 5$. The body force that drives the flow is such that $Re_0 = 64$.

4 | RESULTS

4.1 | Steady simple shear simulations

The response of clamped flexible cylinders to shear flow is shown in Figure 2. One observes increased bending with increased rescaled velocity $\tilde{v}$. Increased bending leaves more room for the shear flow above the cylinders. This reduces the shear rate and—as a

consequence—the shear stress. This apparent shear-thinning effect as a function of geometrical and process parameters has been documented experimentally in great detail in Alvarado et al.[10] Approximately universal behavior was observed when plotting the rescaled impedance $\tilde{Z}$ as output parameter versus $\tilde{v}$ as input parameter. Impedance has been defined as $Z \equiv \tau/U_w$ with τ the shear stress at the top surface, which is a measurable quantity.[10] Rescaled impedance is[10] $\tilde{Z} \equiv \frac{Z - Z_\infty}{Z_0 - Z_\infty}$ with Z_0 and Z_∞ the impedance under near-zero and infinite shear, respectively. In the experiments,[10] Z_0 has been determined by averaging data measured at $\tilde{v} \approx 0.1$, while the determination of Z_∞ involves a fit parameter. Since we do not have extensive simulation data in the $\tilde{v} \approx 0.1$ range and want to avoid the use of a fit parameter, we base our estimates of Z_0 and Z_∞ on the space available for fluid shear above the hair beds at very low shear when the hairs hardly bend and at very high shear when they lie almost flat on the bottom surface: $Z_0 = \rho\nu/(H - \ell)$ and $Z_\infty = \rho\nu/(H - d)$.

We plot the relationship between $\tilde{v}$ and $\tilde{Z}$ obtained from simulations in Figure 3 in the same manner as was presented in Alvarado et al[10] (their Figure 1c). Figure 3 also shows model results from Alvarado et al[10] that were shown to closely follow the experimental data. The simulation results correctly show the transition toward a reduction of impedance that sets in at $\tilde{v} \approx 1$ and for larger $\tilde{v}$ scales as $\tilde{Z} \sim \tilde{v}^{-1/2}$. The set of simulations presented in Figure 3 includes a number of parameter variations: a hexagonal versus a square arrangement of cylinders, variation in surface coverage ϕ, as well as in aspect ratios. We observe that $\tilde{v}$ as an overarching input parameter captures the overall trend in simulated impedance well, as it does in the experimental work.[10]

The simulations being slightly below the model line for $\tilde{v} < 1$ is due to the way we have determined Z_0: without taking into account the effect of flow penetration in an undeformed hair bed. An estimate of the penetration depth that involves—among more—surface coverage by Alvarado et al,[10] supplementary material, results in a reduction of impedance by a factor 0.75–0.95 (for $0.1 \leq \phi \leq 0.3$), which are values for $\tilde{Z}$ actually observed in the low end of $\tilde{v}$ in Figure 3.

It is clear from Figure 2 that the simulations go beyond the small deformations limit. However, the results in Figure 3 indicate that also for larger deformations the simulations capture the essential features of the fluid–structure interaction.
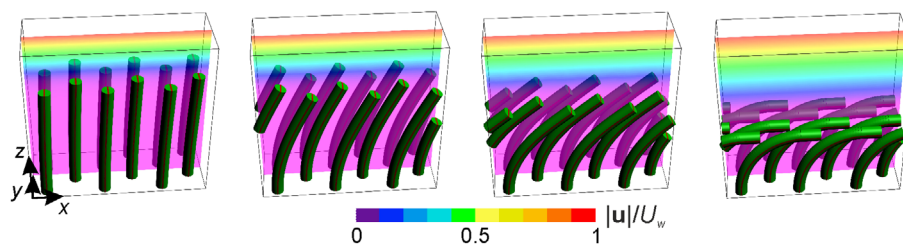

FIGURE 2 Fibers in a hexagonal arrangement bending in simple shear. From left to right the reduced velocity is $\tilde{v} = $ 0.234, 2.34, 4.58, 11.7, respectively. All cases have $\phi = 0.11$, $\ell/d = 10$, and $\ell/H = 0.73$. The panels show three hexagonal unit cells. The periodic condition in x-direction makes that parts of fibers that cross the $x = L$ boundary reappear at the $x = 0$ boundary [Color figure can be viewed at wileyonlinelibrary.com]
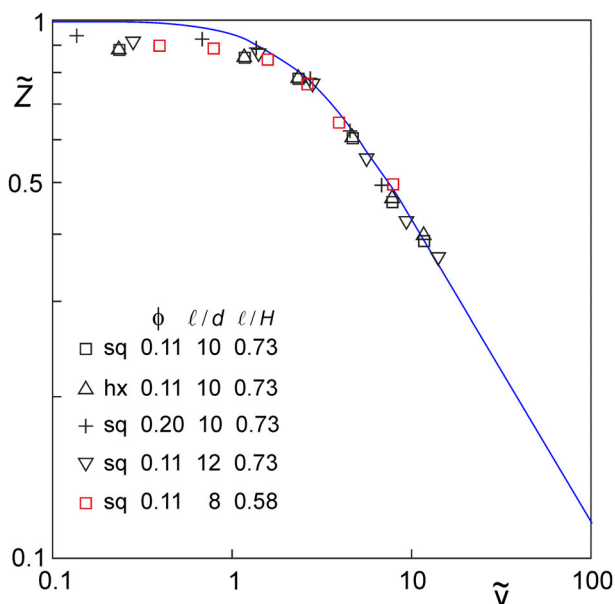
FIGURE 3   Rescaled velocity $\tilde{v}$ versus rescaled impedance $\tilde{Z}$ for soft hair beds experiencing simple shear. The symbols represent simulations in various geometrical systems as indicated—where *sq* is a square pattern of hairs and *hx* a hexagonal pattern. The blue curve is a model due to Alvarado et al.[10] In Alvarado et al,[10] it has been shown that experiments closely follow the model curve [Color figure can be viewed at wileyonlinelibrary.com]

We thus conclude that the simulations are able to reproduce experimental results on cylinders bending under the influence of steady laminar fluid flow. In the remainder of this section, we will explore situations where the flow gets unsteady—but remains laminar—as a result of vortex shedding by the cylinders.

4.2 | Two-dimensional vortex shedding results

Before presenting and discussing vortex shedding results of three-dimensional simulations with flexible cylinders, we first make a brief excursion into two-dimensional simulations on the flow around cylinders in periodic domains. This allows us to relate to the literature on vortex shedding behind multiple cylinders and will help in interpreting the three-dimensional results. The situation is as sketched in Figure 4 (top-right panel). Given the periodic and two-dimensional nature of the simulations, we are dealing with a rectangular array of infinitely long (in the third, *z*-direction) rigid cylinders that are exposed to a cross flow. This is a situation akin to flow around side-by-side cylinders, tube bundles, and "coupled wakes" that have been studied in the literature.[13] Coupled wakes give rise to fluctuation patterns that—as opposed to the wake behind a single cylinder—potentially have multiple frequencies[24] and go through Hopf bifurcations.[13] Next to the Reynolds number, the literature results indicate that the transverse distance of cylinders (the gap ratio[13]) is a parameter that strongly influences the dynamic behavior of the wake flow. For this

reason, we study the effect of the domain width *W* on the wake dynamics.

The flow in the two-dimensional simulations is driven by a body force that has been chosen such that a Reynolds number of approximately $\mathrm{Re} \approx 44$ is achieved. There are methods for controlling the body force such that the Reynolds number precisely attains a certain value.[25] It was, however, decided not to apply such methods as they might result in a slightly fluctuating body force that could interfere with the natural fluctuations of the flow system.

Figure 4 shows a range of vortex shedding scenarios as a function of the width *W* of the periodic domain. The spectra presented in Figure 4—and also later in the article—are based on time series after the instability has reached a dynamically steady state having a length of at least $10d^2/\nu$. The spectral response of the flow to the presence of the cylinder is a marked function of domain width. At $W/d = 5$ there is vortex shedding with a single frequency and thus one Strouhal number. Increasing the domain width induces multiple shedding frequencies to occur simultaneously and the vorticity fields to be more complex. At $W/d = 17.5$, the system again tends to a single Strouhal number that, however, is lower (by almost a factor of two) than for $W/d = 5$. The time series shows some level of irregularity that reflects back as minor peaks in the power spectral density.

As is clear from the vorticity fields shown in Figure 4, as a result of the periodic boundaries in streamwise direction, the flow impacting on the cylinder is unsteady and complex as a result of the unsteady wake of the "upstream" cylinder—which in fact is the cylinder itself. This interaction between the cylinders in the streamwise—but also in the spanwise direction—leads to complex vorticity fields.

In the literature, two-dimensional simulations have probed vortex shedding behind side-by-side cylinders with various cross-sectional shapes[13] as well as cylinders arranged in periodic configurations[26] with an emphasis on the effect of the spacing between cylinders on the dynamics of vortex shedding. It is reassuring to see multi-peak spectra appearing[24] dependent on gap widths and Reynolds numbers with Strouhal numbers comparable to those observed in Figure 4.

For an isolated cylinder with circular cross section, the generally agreed critical Reynolds number for the onset of vortex shedding is $\mathrm{Re} \approx 47$.[27] For cylinders in periodic arrays as well as in side-by-side configurations, the critical Reynolds number can get well below those for isolated cylinders.[24] This is also what we observe in Figure 4.

4.3 | Pressure-driven shear flow with periodic conditions in streamwise and spanwise direction

Figure 5 gives an impression of the flow in the base-case geometry around a rigid cylinder, exposed to planar Poiseuille flow at Re = 27.1. The vorticity field in the mid-*xy*-plane indicates mild vortex shedding, i.e. a minor meandering of the wake behind the cylinder. The isometric view of the velocity magnitude contours shows the three-dimensionality of the flow with relatively high velocities (up to two times the superficial velocity) at lateral periodic boundaries (i.e. in the lateral space between the periodically placed cylinders), boundary
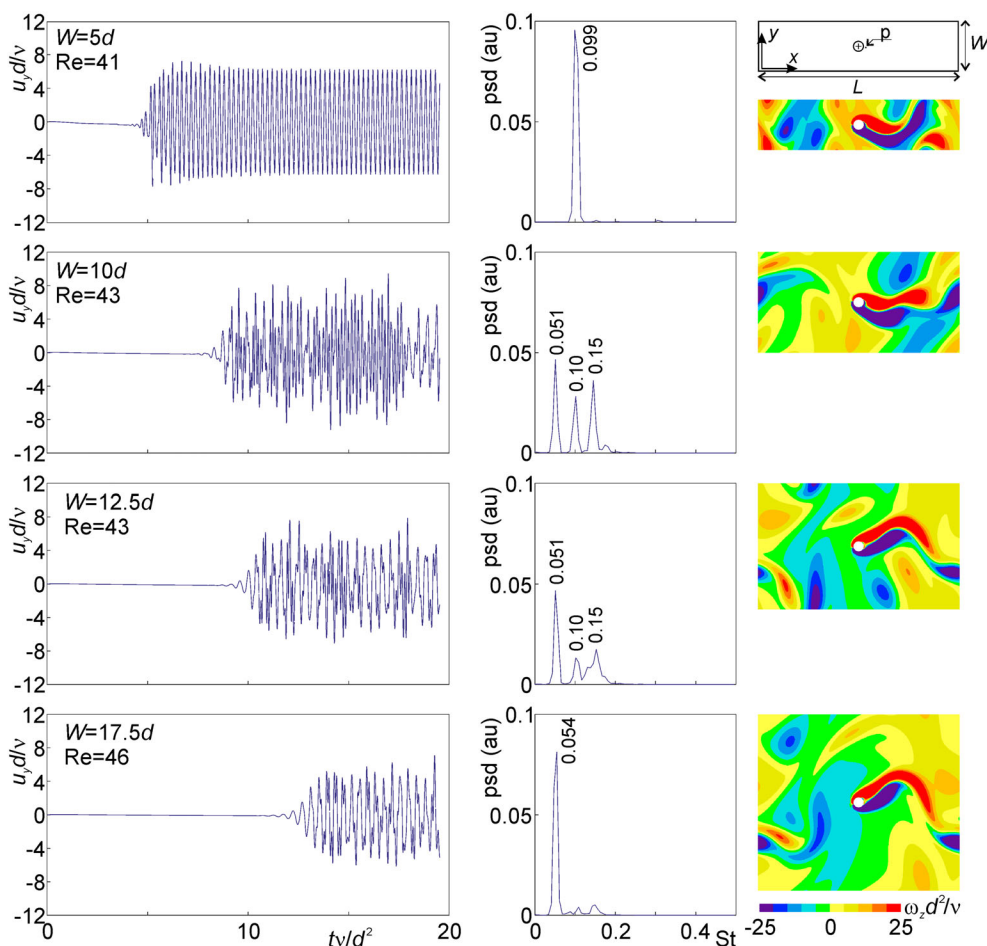
FIGURE 4 Two-dimensional simulations in periodic domains with length $L = 20d$ and width W as indicated. Top right: geometry, coordinate system, and monitor point p. From left to right: time series of dimensionless y-velocity in the monitor point; the corresponding power spectral density; an instantaneous z-vorticity field at a moment when u_y in the monitor point peaks. Reynolds numbers as indicated [Color figure can be viewed at wileyonlinelibrary.com]
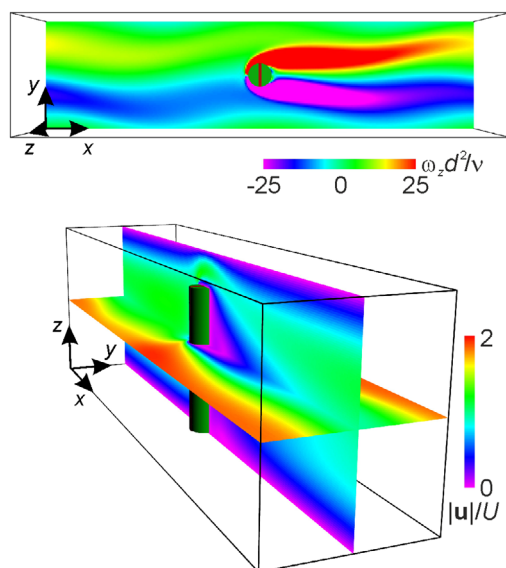

FIGURE 5 Instantaneous realizations of the three-dimensional flow around a clamped rigid cylinder. Top: z-component of the vorticity in the plane $z = H/2$. Bottom: velocity magnitude in the planes $z = H/2$ and $y = W/2$ Base-case geometry with Re = 27.1 [Color figure can be viewed at wileyonlinelibrary.com]

layers at the upper and lower wall with the upper boundary layer perturbed by the flow over the tip of the cylinder, and a three-dimensional wake characterized by low-velocity magnitudes.

For this specific geometry, the onset of vortex shedding is at a Reynolds number in the interval of Re = 20–22, see Figure 6 that shows time series of the velocity in lateral (y) direction in a monitor point in the near wake of the cylinder. For the range of Reynolds numbers investigated (up to Re $\approx$ 35), vortex shedding occurs with a single frequency with—beyond the critical Reynolds number—the Strouhal number only weakly dependent on the Reynolds number at St $\approx 0.12 - 0.13$. This Strouhal number is not that much different from the two-dimensional result with the same streamwise and lateral domain size as used in the 3D simulation—as shown in the top panels of Figure 4—which has St = 0.099. This merely demonstrates that the superficial velocity is an appropriate velocity scale to be used in the Strouhal number in the 3D simulations.

As also shown in Figure 6, the Reynolds number based on the superficial velocity monotonically—though non-linearly—increases with Re_0. Overall Re $\leq 0.5 Re_0$, which indicates that roughly 50% or more of the resistance to flow can be attributed to the cylinder, and the remainder to the channel walls.
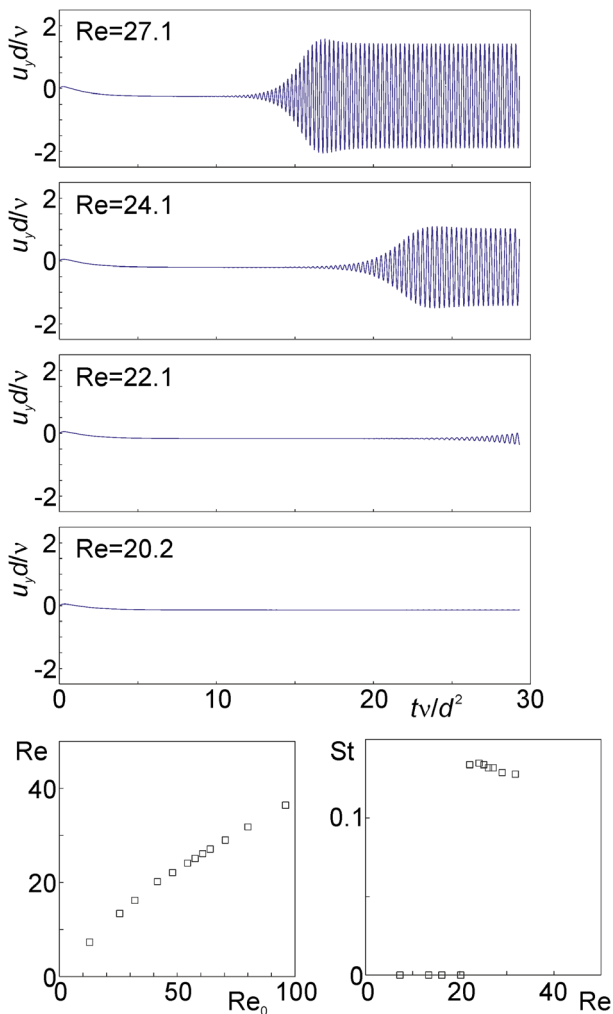
FIGURE 6 Top four panels: time series of (dimensionless) transverse velocity (u_y) in the near wake of a rigid clamped cylinder ($x = L/2 + 5d/4$, $y = W/2 − d/16$, $z = H/2$). Bottom two panels: Re as a function of Re_0 and St as a function of Re. Base-case geometry [Color figure can be viewed at wileyonlinelibrary.com]

FIGURE 7 Instantaneous realizations of the three-dimensional flow around a clamped flexible cylinder with χ = 3.94. Top: z-component of the vorticity in the plane $z = H/2$. Bottom: velocity magnitude in the planes $z = H/2$ and $y = W/2$ base-case geometry at Re = 25.8 [Color figure can be viewed at wileyonlinelibrary.com]

Flexibility of the cylinder has quite an impact on the flow field, including the vortex shedding process. In Figures 7 and 8, we look in detail to one situation that only differs from the rigid cylinder case of Figures 5 and 6 in terms of flexibility. The flexibility parameter is $\chi = \rho U^2 \ell^4 / EI = 3.94$. We note that the Reynolds number for the flexible case is slightly lower than for the rigid cylinder, Re = 25.8 (flexible) versus 27.1 (rigid). Given that the body force driving the flow is the same in the two situations, this means that flexibility has slightly increased the flow resistance. This is an effect opposite to the drag reduction observed in the (steady) shear flow systems discussed earlier. As can be seen in the single realization in Figure 7 and in the time series in Figure 8, the cylinder bends in the flow direction and reaches—after $t \approx 10d^2/\nu$—a deflection in streamwise direction of $w_x \approx d$ along with minor periodic fluctuations in w_x. This bending in the flow direction in itself would reduce flow resistance but this is apparently more than compensated for by increased resistance as a result of the lateral bending motion of the cylinder. We note that—as before in the
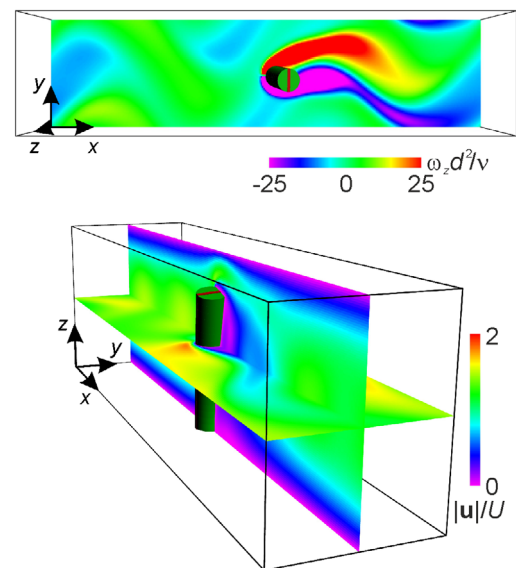
simple shear system—the simulations go beyond the small deformations assumption, which we justify by the favorable agreement with empirical data as shown in Figure 3.

In terms of fluid flow (see Figure 7), the flexible cylinder has a shorter wake and a smaller vortex shedding wavelength as compared to the rigid cylinder (Figure 5).

The bending motion for this specific case is rather complex; see the middle panel of Figure 8 that shows the trajectory the tip of the cylinder is going through in x and y directions. It is a periodic motion, i.e. the same trajectory is traveled over and over again. The power spectral density of the tip deflection in y direction (w_y) is shown in the right panel of Figure 8; it has two distinct peaks (at St = 0.13 and 0.38) and one minor peak (at St = 0.65). As shown in the same figure, the spectrum of the velocity component in y-direction (u_y) in the monitor point defined in Figure 6 closely follows the w_y defection spectrum. The first spectral peak at St = 0.13 is at the same location as the one found for a rigid cylinder. The cylinder's flexibility thus adds additional frequencies to the velocity and deflection fluctuation levels. It needs to be noted here that the frequencies observed so far are well below the first eigenfrequency of the flexible cylinder: $f/f_{n1} \approx \frac{\text{St}}{2\pi \cdot 1.875^2} \cdot \sqrt{\frac{\pi}{4} \frac{\rho_s}{\rho} \chi}$. With a typical density ratio of $\rho_s/\rho = 2$, $\chi = 3.94$ and the highest Strouhal number discernable in Figure 8 (St = 0.65), $f/f_{n1} \approx 0.07 \ll 1$. It also is important to realize that—given the periodic conditions in streamwise and lateral direction—we are dealing with arrays of cylinders moving in perfect phase with frequencies that depend on cylinder (ℓ/d) aspect ratio and the spacing/arrangement of the cylinders, i.e. on the periodic domain size. In short, the systems are very specific, which makes it difficult to cover a full geometrical, material properties, and flow properties parameter space. In what
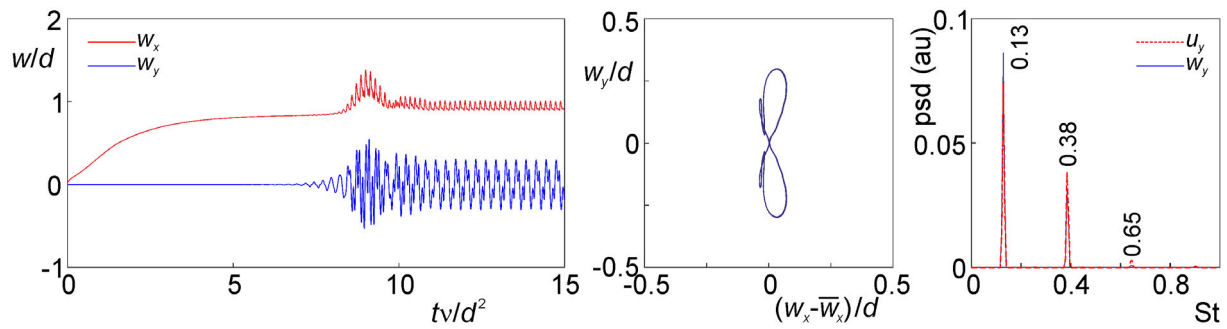
FIGURE 8   Left: onset of the instability in terms of the end-point deflection in streamwise and spanwise directions w_x and w_y as a function of time. Middle: path traveled by the endpoint after periodic motion has set in (with $\bar{w}_x$ the time-averaged x-deflection). Right: power spectral density of the w_y signal and the transverse velocity u_y in the same monitor point as used in Figure 6. Base-case geometry at $\chi = \rho U^2 \ell^4 / EI = 3.94$ and Re = 25.8 [Color figure can be viewed at wileyonlinelibrary.com]
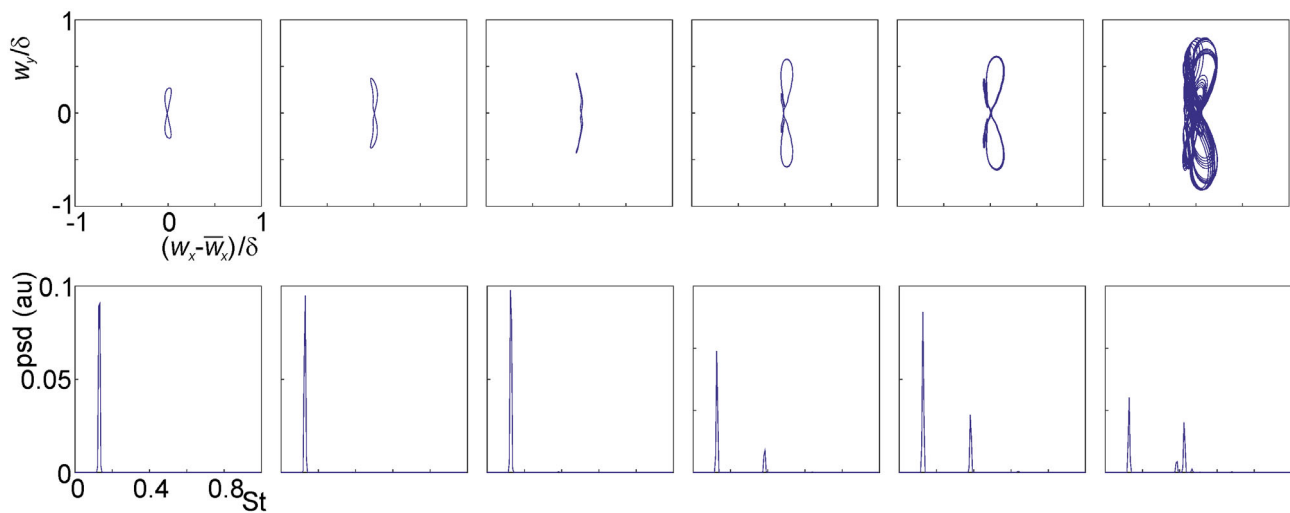

FIGURE 9   Cylinder tip deflection $w_x - \bar{w}_x$ versus w_y normalized by $\delta = \frac{1}{8}\rho U^2 d\ell^4 / EI$ (top row) and power spectral density of w_y (bottom row) with—from left to right—increasing flexibility $\chi = 0.156$, 1.49, 2.20, 3.70, 3.94, and 4.16, respectively. In all cases $\text{Re}_0 = 64$, while Re = 27.0, 26.4, 26.2, 25.9, 25.8, and 25.5 (from left to right). Base-case geometry [Color figure can be viewed at wileyonlinelibrary.com]

follows, we will be mainly focusing on the effect of the cylinder flexibility (i.e. the parameter χ) for two domain widths W. Involving domain width is motivated by the observations we made for two-dimensional cases that are shown in Figure 4.

In Figure 9, we study the role of flexibility on the bending motion of the cylinder in the base-case configuration that—among more—has $W/d = 5$. We keep the flow system—geometry, driving force, fluid properties—the same and only vary the bending stiffness EI of the cylinder. We plot the trajectory of the cylinder tip as well as the w_y spectra. So far, we have scaled cylinder deflections with the diameter of the cylinder (w_x/d and w_y/d). In order to facilitate comparison of simulations over a wide range of bending stiffness, the deflections w_x and w_y are from now on scaled with the deflection $\delta = \frac{1}{8}\rho U^2 d\ell^4 / EI$ a clamped cylinder would experience if it were loaded with a uniform force per unit length equal to $q = \rho U^2 d$.

As noted in the caption of Figure 9, there is a weak but consistent decrease in the Reynolds number based on the superficial velocity with increased flexibility of the cylinder, that is, an increased

resistance to flow with increased flexibility. Given that the lateral deflections scaled with δ increase with increasing flexibility makes that the lateral bending more than proportionally increases with flexibility χ. For the highest value of χ considered in Figure 9 ($\chi = 4.16$), the trajectory of the tip of the cylinder ceases to be periodic.

All simulations in Figure 9 show a principal frequency of the bending motion w_y of St = 0.13. Between $\chi = 2.20$ and 3.70, a second spectral peak appears at St = 0.38. For $\chi = 4.16$, additional frequencies can be observed.

At this stage, it is important to ascertain that the effects observed are of a physical, as opposed to a numerical, nature. For this, we have looked into the effects of time and space resolution on the results of the simulations. When it comes to time resolution, the default simulations have a kinematic viscosity of $\nu = 0.025$ in lattice units ($\Delta^2/\Delta t$). With the default spatial resolution such that the cylinder diameter is spanned by 16 lattice spacings $d = 16\Delta$, this implies that one viscous time scale $d^2/\nu = 10240\Delta t$. If we increase the viscosity and keep $d = 16\Delta$, we thus decrease the number of time step per viscous time
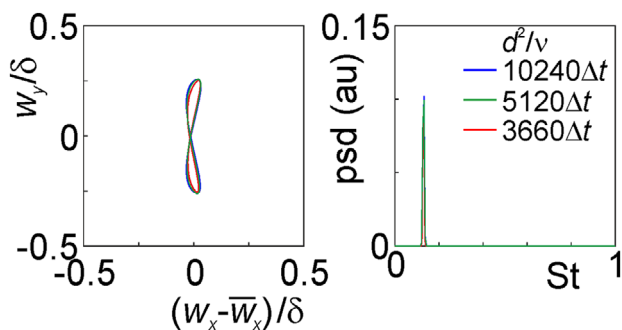
FIGURE 10 Effect of time step on tip deflection (left) and power spectral density of w_y (right). Base-case geometry with $Re_0 = 64$. In all three cases $Re = 27.1 \pm 0.1$ and $\chi = 0.0157 \pm 0.002$ [Color figure can be viewed at wileyonlinelibrary.com]

scale, which means increasing the time step in physical terms. In Figure 10, we show a comparison between three simulations that all are identical in terms of dimensionless input parameters and spatial resolution but that have different physical time step. We see good agreement of the trajectory traveled by the tip of the cylinder as well as of the w_y spectrum. The Strouhal numbers of the spectral peaks are within 0.01, where the resolution of the spectra is $\Delta St \approx 0.005$. As indicated in the caption of Figure 10, the Reynolds numbers—based on the superficial velocity—of the three simulations are within 0.1.

The effects of spatial resolution ($d = 12\Delta$, 16Δ, 24Δ) have been tested for two different values of the flexibility ($\chi \approx 2.2$ and $\chi \approx 3.9$); the results are shown in Figure 11. The superficial velocities are such that the Reynolds numbers associated with the various resolutions agree within 1% and 1.5% for $\chi \approx 2.2$ and 3.9, respectively. The spectra largely overlap. There is a weak trend with resolution when it comes to the path traveled by the cylinder tip: for both flexibilities, increasing the resolution leads to a weak decrease in the amplitude of the motion of the tip in y-direction. The amplitudes for $d = 16\Delta$ and 24Δ, however, differ by less than 1%.

We thus observe decent grid size and time step size independence, which then justifies the default lattice spacing and time step that are defined by $d = 16\Delta$ and $d^2/\nu = 10240\Delta t$, respectively.

The spectral results of a significant set of simulation for a range of flexibility parameters and for two domain widths W are summarized in Figure 12. We show the location of main spectral peaks as a function of χ. Looking at the relatively narrow system with $W/d = 5$ first, we see a few step-changes/bifurcations. The single Strouhal number $St = 0.13$ that is associated with vortex shedding behind a rigid cylinder persists until $\chi \approx 4.5$. At $\chi \approx 3.3$, however, a second frequency at $St = 0.38$ appears in the spectrum. We noted before (Figure 9) that beyond $\chi = 4$ the motion of the cylinder tip is not periodic anymore. This transition is associated with a small shift of the high frequency from $St = 0.38$ to $St = 0.42$. At the highest level of flexibility we simulated, $\chi = 5.6$, we observe a spectrum with four distinct peaks, as shown as an inset in the left panel of Figure 12.

A similar series of simulations were performed for a wider domain: $W/d = 7.5$. Here we have included a rigid cylinder ($\chi = 0$)
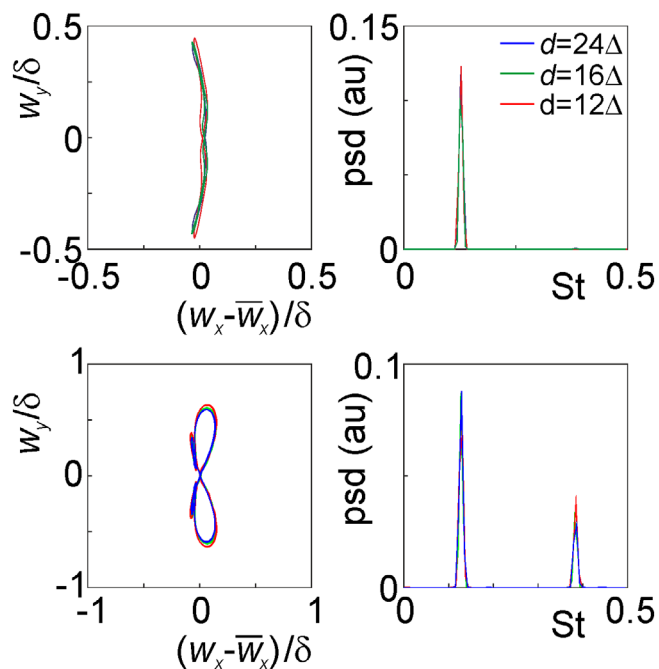

FIGURE 11 Effect of spatial resolution (in terms of number of grid spacings Δ spanning d) on tip deflection and (left) power spectral density of the w_y signal (right). Base-case geometry with $Re_0 = 64$. Top: $\chi = 2.20 \pm 0.02$; bottom $\chi = 3.94 \pm 0.05$ [Color figure can be viewed at wileyonlinelibrary.com]
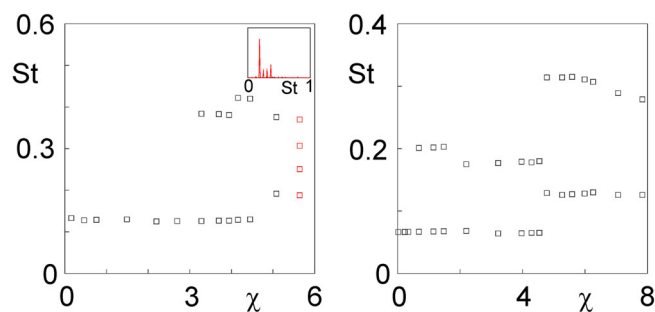

FIGURE 12 Frequencies associated to peaks in the power spectral density of the w_y signal as a function of flexibility parameter χ. Left: base-case conditions, including a domain width of $W = 5d$; right: same as left except that now $W = 7.5d$. The inset in the left panel is the spectrum at $\chi = 5.6$, which has four frequencies represented by the four red symbols [Color figure can be viewed at wileyonlinelibrary.com]

result. The (only) frequency $St = 0.067$ associated to that simulation persists until $\chi = 4.5$. From $\chi = 0.68$, however, this base frequency is joined by higher frequencies, first $St = 0.20$, later $St = 0.18$. At $\chi = 4.5$, there is a bifurcation into a flow system with a low frequency of $St \approx 0.13$ and a second frequency that starts at $St \approx 0.31$ and gradually decays to $St = 0.28$ when the flexibility parameter has become $\chi = 7.8$.

From the above exercise, we see that bending stiffness adds complexity to the vortex shedding process with oscillations that eventually

become quasi-periodic. Given the numerical (time and space resolution) checks that have been performed, we deem the scenarios observed of a physical nature and will welcome experimental results that may confirm or falsify the numerical results.

5 | SUMMARY, CONCLUSIONS, AND OUTLOOK

In this article, we have performed fully resolved simulations of soft hair beds bending under the effect of a laminar shear flow. The inspiration comes from experimental work due to Alvarado et al[10] and has been extended toward situations where the hairs (flexible cylinders attached to a solid wall) facilitate vortex shedding. The simulations represent the experimentally observed flow response of the soft hair beds well and thereby confirm the scaling properties of the response. In this scaling, the surface coverage fraction ϕ and the hair aspect ratio ℓ/d play prominent roles.

Two-dimensional simulations of vortex shedding in periodic domains highlight the impact the domain size (i.e. the spacing between cylinders) has on the spectral response, in agreement with findings from the literature on flow past multiple cylinders of various cross-sectional shape and in various arrangements.

The three-dimensional planar Poiseuille flow simulations with a cylinder attached to one of the walls have been verified with respect to the numerical settings. Time-step coarsening and grid coarsening and refinement have marginal effects on the bending motion of the cylinder, even under challenging conditions when the trajectory traveled by the cylinder tip shows fine detail and multiple frequencies.

Cylinder flexibility has significant impact on the vortex shedding process. Most importantly it adds frequencies to its spectral behavior. It also—weakly—adds to the flow resistance of the cylinder. The Poiseuille system goes through a number of bifurcations when increasing the flexibility of the cylinder. It was demonstrated that the bifurcation scenarios strongly depend on the domain width and thus—given the periodic nature of the simulations—the spacing between cylinders. The periodic boundary conditions in streamwise and spanwise directions make that all periodic copies of the cylinder deform in-phase. By performing simulations with two side-by-side cylinders and two cylinders aligned in the streamwise direction, we will be investigating—through simulation—the consequences of deviations from periodicity on the temporal behavior of the cylinders' deformations.

A clear challenge in the study we have performed is a meaningful variation of parameters. The dimensionality of the parameter space is large, specifically with respect to flow geometry and flow conditions. As also noted above, experimental data—specifically covering the vortex shedding regime—will be very useful for validation as well as for guidance toward relevant parameter variations.

Given that in biology soft hair beds are considered to have a function in regulating mass transfer (e.g. in blood vessels), future work that involves adding scalar transport to the fluid–structure interaction simulations described above will be a very interesting avenue for future research. In nature, active soft hair beds (motile cilia[28,29]) generate fluid flow—for example, for enhancing mass transfer or for locomotion—by performing a collective, wave-type deformation. The simulation methodology as described and used in this article is well suited to investigate such metachronal waves in detail.

AUTHOR CONTRIBUTIONS

Jos Derksen: Conceptualization; investigation; methodology; writing-original draft; writing-review & editing.

DATA AVAILABILITY STATEMENT

The data that support the findings of this study are available from the corresponding author upon reasonable request.

ORCID

Jos J. Derksen https://orcid.org/0000-0002-9813-356X

REFERENCES

1. Vernekar R, Krüger T. Breakdown of deterministic lateral displacement efficiency for non-dilute suspensions: a numerical study. *Med Eng Phys*. 2015;37:845-854.
2. Dupin MM, Halliday I, Care CM, Alboul L, Munn LL. Modeling the flow of dense suspensions of deformable particles in three dimensions. *Phys Rev E*. 2007l;75:066707.
3. Albayrak I, Nikora V, Miler O, O'Hare MT. Flow-pant interactions at leaf, stem and shoot scales: drag, turbulence and biomechanics. *Aquat Sci*. 2013;76:269-294.
4. Zhang X, Nepf H. Wave-induced reconfiguration of and drag on marsh plants. *J Fluids Struct*. 2021;100:103192-1–20.
5. Opinel P-A, Srinil N. Application of wake oscillators to two-dimensional vortex-induced vibrations of circular cylinders in oscillatory. *J Fluids Struct*. 2020;96:103040.
6. Nakatani Y, Suzuki K, Inamuro T. Flight control simulations of a butterfly-like flapping wing–body model by the immersed boundary–lattice Boltzmann method. *Comput Fluids*. 2016;133:103-115.
7. Deshpande P, Modani A. Experimental investigation of fluid–structure interaction in a bird-like flapping wing. *J Fluids Struct*. 2019;91: 102712.
8. du Roure O, Lindner A, Nazockdast EN, Shelley MJ. Dynamics of flexible fibers in viscous flows and fluids. *Annu Rev Fluid Mech*. 2019;51: 539-572.
9. Son K, Guasto JS, Stocker R. Bacteria can exploit a flagellar buckling instability to change direction. *Nat Phys*. 2013;9:494-498.
10. Alvarado J, Comtet J, de Langre E, Hosoi AE. Nonlinear flow response of soft hair beds. *Nat Phys*. 2017;13:1014-1019.
11. Batchelor GK. *An Introduction to Fluid Mechanics*. Cambridge: Cambridge University Press; 1967.
12. Derksen JJ. Suspension of flexible cylinders in laminar liquid flow. *AIChE J*. 2020;66:pe16952.
13. Peng YF, Sau A. Transitional hysteresis loop and coexistence of synchronized shedding in coupled wakes. *Phys Fluids*. 2015;27:074104.
14. Tong F, Cheng L, Zhao M, Zhou T, Chen X-B. The vortex shedding around four circular cylinders in an in-line square configuration. *Phys Fluids*. 2014;26:024112.
15. Ma S, Kang C-W, Lim T-BA WC-H, Tutty O. Wake of two side-by-side square cylinders at low Reynolds numbers. *Phys Fluids*. 2017;29: 033604.
16. Meirovitch L. *Analytical Methods in Vibrations*. New York: Macmillan; 1967.
17. Somers JA. Direct simulation of fluid flow with cellular automata and the lattice-Boltzmann equation. *Appl Sci Res*. 1993;51:127-133.

18. Eggels JGM, Somers JA. Numerical simulation of free convective flow using the lattice-Boltzmann scheme. *Int J Heat Fluid Flow*. 1995;16: 357-364.

19. Succi S. *The Lattice Boltzmann Equation for Fluid Dynamics and Beyond.* Oxford: Oxford University Press; 2001.

20. Peskin CS. Flow patterns around heart valves—numerical methods. *J Comput Phys*. 1972;10:252-271.

21. Ten Cate A, Nieuwstad CH, Derksen JJ, Van den Akker HEA. PIV experiments and lattice-Boltzmann simulations on a single sphere settling under gravity. *Phys Fluids*. 2002;14:4012-4025.

22. Timoshenko SP, Gere JM. *Mechanics of Materials*. New York: Van Nostrand Reinhold; 1973.

23. Derksen JJ. Liquid fluidization with cylindrical particles: highly resolved simulations. *AIChE J*. 2019;65:e16594.

24. Bai X-D, Zhang W, Guo A-X, Wang Y. The flip-flopping wake pattern behind two side-by-side circular cylinders: a global stability analysis. *Phys Fluids*. 2016;28:044102.

25. Jain R, Tschisgale S, Froehlich J. Effect of particle shape on bedload sediment transport in case of small particle loading. *Meccanica*. 2020; 55:299-315.

26. Balachandar S, Parker SJ. Onset of vortex shedding in an inline and staggered array of rectangular cylinders. *Phys Fluids*. 2002;14:3714-3732.

27. Espinosa-Gayosso A, Ghisalberti M, Ivey GN, Jones NL. Particle capture by a circular cylinder in the vortex-shedding regime. *J Fluid Mech*. 2013;733:171-188.

28. Nawroth JC, van der Does AM, Ryan (Firth) A, Kanso E. Multiscale mechanics of mucociliary clearance in the lung. *Philos Trans R Soc B*. 2019;375:20190160.

29. Gu H, Boehler Q, Cui H et al. Magnetic cilia carpets with programmable metachronal waves. *Nat Commun* 2020; 11: 2637.